Visualized high-T_c superconducting mechanism of polyhedral quantum wells confined electrons

Xiuqing Huang[1,2,*]

[1]Department of Telecommunications Engineering ICE, Army Engineering University, Nanjing 210007, China
[2]National Laboratory of Solid State Microstructures, Nanjing University, Nanjing, 210093, China
[*]e-mail: xiuqing_huang@163.com

ABSTRACT

Despite decades of research, the origin of high-temperature superconductivity is still unclear, and its microscopic mechanism remains a subject of intense debate. The intrinsic Mott insulating properties of copper oxide parent compounds and the experimentally observed charge-ordered phases in real space suggest that high-temperature superconductivity may stem from localized electrons rather than itinerant electrons. In this work, we propose a unified microscopic mechanism where confined electrons within polyhedral quantum wells represent the Mott ground state, and symmetry-breaking of electron-hole pairs acts as the superconducting mechanism. A single parameter formula for the critical temperature (T_c) of unconventional superconductors is developed, allowing accurate determination of T_c based on lattice constants. The approach elucidates relationships between various charge-order phases and doping concentration, explores Fermi surface structures, investigates spin resonance peaks and parities, and examines pressure-induced dual superconducting phase transitions - all consistent with experimental observations. It is also estimated that the highest T_c of the newly discovered nickel-based superconductor will not exceed 100 K. This work offers critical insights into unconventional superconductivitys fundamental mechanisms while introducing a new paradigm to reveal more intrinsic connections between superconductivity, conductivity, and magnetism.

Introduction

The discovery of superconductivity by Onnes in 1911 marked a landmark achievement in physics[1]. Decades later, the BCS theory explained this magical phenomenon, attributing it to the formation of Cooper pairs through electron-phonon interactions[2]. However, the emergence of high-temperature superconductors (HTS), such as those based on copper[3–5], iron[6–8], and most recently discovered nickel[9], posed a formidable challenge to established theories. One of the big challenges to understanding these materials is that the conventional model of electron motion in solids no longer holds true[10,11]. The need for lattice vibration mediation in superconductivity and whether Cooper pair formation requires a bosonic glue has been widely questioned[12,13]. Despite extensive research into these compounds' unique properties and underlying mechanisms, no compelling replacement has yet garnered widespread acceptance[14,15].

The STM results suggest that doped antiferromagnetic Mott insulators exhibit a strong propensity towards forming real-space charge patterns or stripes[16–20], sparking a heated debate on how electrons behave in HTS[21,22]. Two opposing viewpoints have emerged from this discussion. Mainstream scholars contend that despite the strong interactions between electrons in HTS, they can still be considered coherent waves propagating through the ion lattice, resulting in well-defined electron states in momentum space. In contrast, minority scholars argue that the strong correlation system is the strong localization of electrons, and the conventional picture is no longer valid. Now, enough experiments support that electrons tend to congregate in quasi-1D charge rivers (stripes) separated by insulating domains[23–25]. In any case, the striped phase implies the key pathway to understanding the nature of the superconducting mechanism[18,26,27]. Developing a proper theoretical framework in a localized (real space) picture rather than an itinerant (momentum space) picture will be a major task for those endeavoring to solve the high-T_c conundrum.

As we know, any superconductor can be simplified into three elements: positively charged ions (A), negatively charged valence electrons (B), and the applied electromagnetic field energy (C). In terms of ABC's ternary system, there exist only two distinct combinations (paradigms): (I) A+(B+C) and (II) (A+B)+C. The first is the BCS paradigm of conventional superconductors, where the external electric field (C) must be coupled with the moving electrons (B) to generate current. Concurrently, the ions (A) must supply the energy (glue) required for electron pairing through continuous vibration (phonons). It is now evident that the first framework cannot describe unconventional superconductors, so the second combination is the only option for strongly correlated electron systems. In the second example, ions (a) and electrons (b) in superconductors self-assemble into the ground state of a Mott insulator through Coulomb interaction, and its most crucial electrical characteristic is that the positive and negative charge centers coincide entirely, and the total capacitance is zero. In short, electrons form an intuitive

picture of Wigner crystals, while the electromagnetic field energy (C) propagates independently. In the external electric field, the electrons are slightly displaced relative to the positive charge background, which leads to the system symmetry breaking along the electric field direction. Currently, superconductors' positive and negative charge centers no longer coincide, showing a non-zero total capacitance and the opening of electromagnetic channels. When $T < T_c$, the thermal vibration of ions and electrons is wholly suppressed; accordingly, the capacitance of the superconductor reaches the maximum, and the electromagnetic field energy can generate a superconducting current through the quasi-one-dimensional stable channels (stripes) established by (A+B) without any loss (zero resistance).

This work proposes an approach to addressing longstanding questions related to microscopic electrons in unconventional superconductors and their connection to macroscopic experimental phenomena. According to the crystal structure parameters, the new mechanism can directly predict the superconducting transition temperatures of copper- and iron-based superconductors. Moreover, the theoretical framework realizes the visualization of microscopic superconducting electronic behavior and offers fresh insights into several important experiments: (1) the formation and evolution of the charged ordered phases (nematic, 1/8 anomaly, checkerboard) in cuprate oxides[28–36]; (2) how doping concentration dictates Fermi surface patterns and their impact on the trilayer $Bi_2Sr_2Ca_2Cu_3O_{10+\delta}$ (Bi2223)[37]; (3) the spin resonance peaks and their association with real-space Cooper-pair harmonic oscillators in the bilayer iron-based $CaKFe_4As_4$ superconductor[38]; and (4) the pressure-induced transfer of Cooper pairs and dual superconducting phase transitions in $K_{0.8}Fe_ySe_2$[39]. Encouragingly, all experimental results can be analytically reproduced under the suggested unified mechanism.

Octahedral quantum well and T_c in copper oxide superconductors

The first high-temperature superconductor was achieved by doping the insulator La_2CuO_4 with Sr/Ba[3]. Here, two fundamental questions are raised: (1) What is the real space structure of the electronic state in the insulator? (2) how does doping cause a transition from an insulating state to a superconducting state? Typically, hole carriers are believed to be generated when divalent Sr or Ba replaces trivalent La, which induces the onset of superconductivity. However, this leads to one new issue: What is the microstructure of holes in real space, and how do they move without resistance in a superconductor?
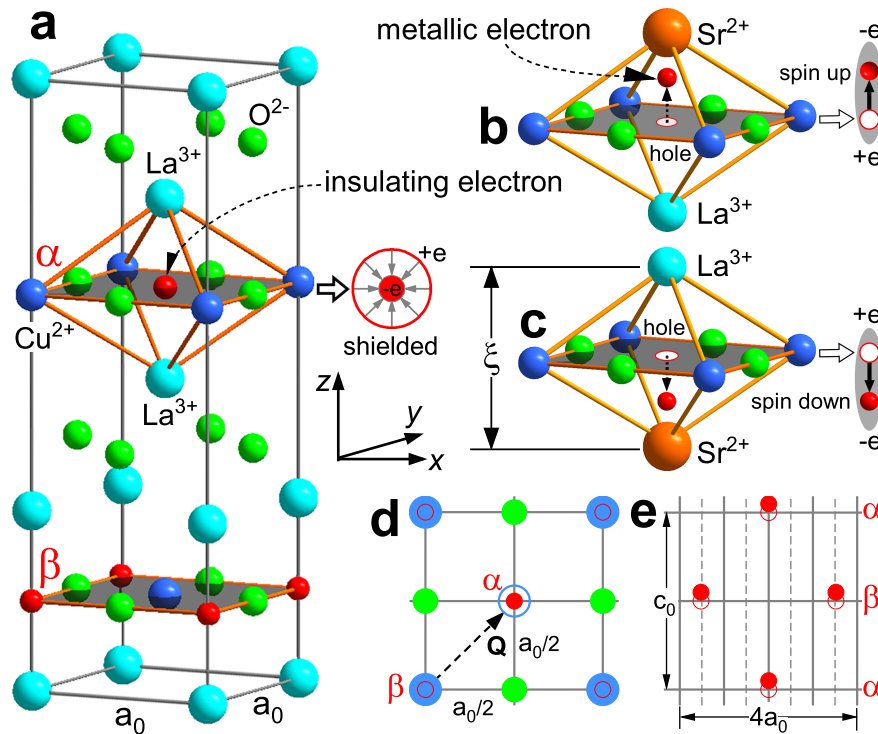
Figure 1. Localized electrons in octahedral quantum well and symmetric breaking in copper oxide superconductor. **a**, Mirror-symmetric octahedral quantum well and shielded insulating electrons in undoped La_2CuO_4. **b-c**, Doping-induced mirror symmetry breaking and the emergence of holes and up and down electron-hole pairs. **d**, Relationship between the $\alpha-$ and $\beta - CuO_2$ layers in **a**, they differ by a displacement vector $\mathbf{Q} = (a_0/2, a_0/2)$. **e**, Three sandwich CuO_2 layers of $\alpha\beta\alpha$, the doped electrons form a symmetric stable Wigner crystal structure of $4a_0 \times c_0$ on the nonsuperconducting xz-plane.

Table 1. The relationship between T_c of copper-based superconductors and the distance ξ between two vertices of octahedral quantum well, the values in bold are possible superconducting phases.

Compound	T_c (K)	ξ_α (Å)	ξ_β (Å)	λ
$Ba_2CuO_{4-\delta}$	73	**3.7338**		1018
$YBa_2Cu_3O_{7-\delta}$	93	**3.6720**		1254
$Bi_2Sr_2Ca_2Cu_3O_{10+\delta}$	110	3.1511	**3.3272**	1217
$TlBa_2CaCu_2O_{7+\delta}$	103	**3.5771**		1317
$TlBa_2Ca_3Cu_4O_{11+\delta}$	112	3.2453	**3.5025**	1373
$TlBa_2Ca_2Cu_3O_{10+\delta}$	120	**3.2381**	3.5305	1258
$Tl_2Ba_2Ca_2Cu_3O_{10+\delta}$	128	**3.3053**	3.5252	1393
$HgBa_2CuO_{4+\delta}$	94	**3.8241**		1374
$HgBa_2Ca_2Cu_3O_{8+\delta}$	134	**3.2108**	3.4241	1380

Fig. 1a shows the undoped La_2CuO_4 single cell in the insulating phase; due to the strong Coulomb confinement from the surrounding lattice ions, the electron is trapped into the CuO_2 plane and becomes localized within the octahedral quantum well. Because the irons of the quantum well are completely symmetrical in *xyz* three directions, the center of positive and negative charges overlap perfectly. As a result, the localized electrons in the octahedron are entirely wrapped and shielded by the +e shell (as illustrated in the right insert), rendering the electrons invisible to external electric fields, so the material appears insulating. Hence, we call these shielded electrons insulating electrons.

To understand how the phase transition is achieved from an insulating state to the metallic and superconducting state, we must consider what happens to the Mott insulator as it is doped with holes. When strontium is doped, the Sr^{2+} substitutes the La^{3+} in two ways. In doping at the upper position (Fig. 1b), because the charge balance of the two vertices and the mirror symmetry of the octahedron is broken, and the electron is pushed upward away from the CuO_2 plane and rests at a new equilibrium position above the plane, leaving behind a hole at its original location. In the way of doping at the lower position (Fig. 1c), analogously, the electron is pushed downward away from the CuO_2 plane, and the original location also forms a hole. Doping leads to symmetry breaking, as shown in the right inset of Fig. 1b and c, which are equivalent to generating upward and downward electron-hole unit electric dipoles, respectively. Furthermore, as indicated in the figure, we can describe these two symmetric broken electronic states by spin up and down. Now the electrons are no longer shielded and can respond to external fields, which we call metallic electrons. It is easily seen that holes are a virtual quasiparticle concept, acting as the shadow of electrons. Since electrons are localized, holes are also localized.

In the framework of localized electrons, the stability of the Wigner crystalline structure formed by electrons in real space directly affects the temperature of the superconducting transition. We find that many experimental phenomena and physical properties of high-temperature superconductors can be quantitatively determined by the crystal structure and octahedral quantum well shown in Fig. 1a. There are usually two copper oxide planes (α and β) within the single cell, their projections on the *xy*-plane differ by vector $\mathbf{Q} = (a_0/2, a_0/2)$ (Fig 1d), which is beneficial for the formation of stable symmetric structures of metallic electrons in the non-superconducting *xz*-plane (Fig 1e). It should be noted that many high-quality copper oxide superconductors have lattice constants satisfying $c_0/a_0 = 4$, such as $Bi_2Sr_2CuO_{6+\delta}$ (Bi2201) with $c_0/a_0 = 4.13$[34], and $Ca_2CuO_2Cl_2$ (CCOC) with $c_0/a_0 = 3.89$[35]. In the following sections, we will further prove that all various charge-ordered phases found in the experiment, especially many STM results with a periodicity of four unit cells[34,35], are all rooted in Fig 1e.

The relationship between crystal structure and superconducting transition temperature is crucial in superconducting research. It has been found that T_c can be manipulated by various means, including applying pressure and substituting elements (chemical pressure) with varying ionic radii. Whether it's mechanical or chemical pressure they mainly shorten the lattice's *c*-axis, meaning that the most crucial effect of pressure is to reduce the octahedral quantum well's ξ of Fig 1b and c, resulting in stronger Coulomb confinement for electrons along the *c*-axis. In other words, the pressure effect can transform macroscopic external pressure into microscopic electronic localization. Based on this analysis, we can speculate that the highest T_c in copper oxide superconductors is inversely proportional to ξ, and smaller ξ values are more likely to achieve higher T_c. The experimental data of different copper oxide superconducting series in Table 1 well supports this hypothesis.

From Table 1, it can be seen that some superconductors have two possible types of octahedral quantum wells with different ξ values, the corresponding ξ values for the superconducting transition phase shown in bold, and different superconducting phases can be distinguished from ARPES and other experiments[37]. Since the superconducting energy gap Δ is directly proportional to the superconducting transition temperature T_c, according to Table 1, we can get the following simple relationships among Δ, T_c and ξ as:

$$\triangle \propto T_c = \frac{\lambda}{\xi^2} \simeq \frac{1300}{\xi^2}, \tag{1}$$

where λ represents the coupling strength between electrons and quantum wells, which is called the correlation strength factor. The average value λ for cuprate superconductors is taken as $\lambda(Cu) = 1300$. The formula clearly shows that with the shrinking of ξ, electrons are more stable in the z-direction, and the material is more likely to achieve a higher T_c.

Doping induced charge order in cuprate superconductors

Increasing evidence shows that layered superconductors exhibit "striped superconductivity", wherein the charge stripe phase is considered quasi-one-dimensional. Moreover, experiments also suggest that superconductivity originates in charge stripes that extend along the b-axis of the crystal, where the superfluid density is substantially larger than for the a-axis direction[40]. According to Fig. 1e, since the charge pattern on the non-superconducting ac-plane is fixed, the change of doping concentration only occurs in the b-axis direction. From the point of view of crystal stability of electrons, we can assume that the quasi-one-dimensional doping in the b-axis is also periodically uniform so that the doping concentration can be expressed as

$$x_n = \frac{2}{4 \times n}, \quad n = 2, 3, 4, \cdots. \tag{2}$$

where n is the charge stripe spacing along the b-axis.
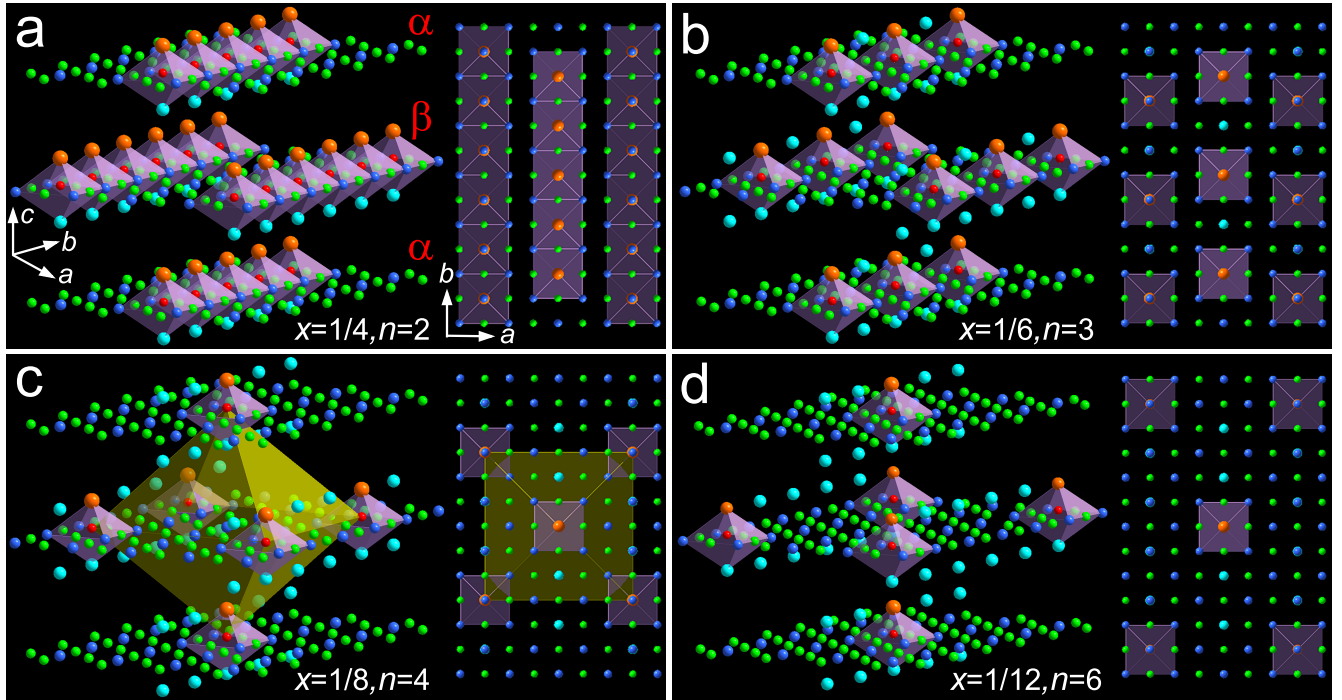
Figure 2. The evolution of the real space quasi-one-dimensional charge ordered structures with the doping concentration in copper oxide superconductors. **a**, When doping level at $x = x_2 = 1/4$, a superconducting state with the highest doping concentration and fully filled quasi-one-dimensional charge stripes. **b**, Optimum doping at $x = x_3 = 1/6$ and semi-filled charge stripes. **c**, In the magic doping $x = x_4 = 1/8$, the electrons form a big octahedral non-superconducting checkerboard charge order, where the electrons are repinned. **d**, Underdoped charge stripes at $x = x_6 = 1/12$.

The physical meaning of the equation (2) is clear, where numerator 2 represents two kinds of CuO$_2$ planes (α and β) along the c-axis, and denominator 4 represents charge stripe spacing along the a-axis. Fig. 2 depicts the four characteristic charge-ordered superconducting states in LSCO. Fig. 2a is the highest hole-doped superdonducting state with $n = 2$ and $x_2 = 0.25$; the top view shows all doping sites are full-filled. Further doping into Fig. 2a would destroy the charge-ordered structure and superconductivity. Fig. 2b shows the optimal doping case with $n = 3$ and $x_3 \approx 0.166$. The top view reveals that
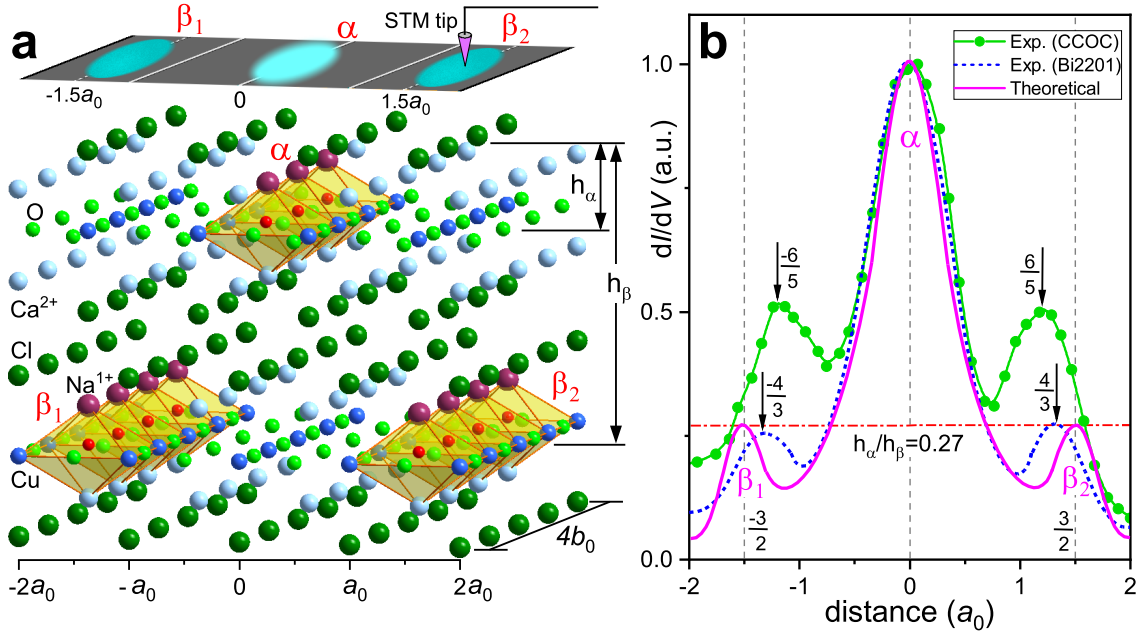
Figure 3. Explanation of local nematic states in Copper-based Superconductors. **a**, In the $4a_0 \times 4b_0$ plaquette of CCOC, the metallic electrons from the three quantum wells (α) in the central of the upper CuO_2 layer contribute to the central brightest bar in the STM experiment, while electrons from the four quantum wells (β_1 and β_2) on both sides of the lower layer contribute to the two sidebars. **b**, The normalized DOS peaks are represented by magenta as theoretical results, with smaller peaks appearing at $\pm 1.5a_0$. The experimental results for CCOC and Bi2201 are shown in green and blue, respectively, with smaller peaks around $\pm 1.2a_0$ and $\pm 1.3a_0$. The red dotted line represents the weak peak value of 0.27, which is determined by the distances (h_α and h_β) between the CuO_2 planes and the cleavage plane.

the corresponding one-dimensional superconducting chains are at half-filling. Fig. 2c represents the well-known 1/8 anomaly. Due to equal charge stripe spacings along the *a*- and *b*-axis directions, a low-temperature orthogonal (LTO) to low-temperature tetragonal (LTT) phase transition occurs, causing electrons to be pinned and restructured into stable yellow octahedra. In this state, the external field cannot induce the symmetry breaking of the electron states, resulting in the superconductor behaving as an insulator. Fig. 2d represents the stripe structure with $n = 6$ and $x_6 \approx 0.083$, corresponding to an underdoped superconducting state. In equation (2), n is not arbitrarily large; if n is too large, the electrons become too sparse and cannot form a stable superconducting charge order through Coulomb repulsion competition. Based on experimental results, the maximum value of n is 8, corresponding to a hole doping concentration of $x_8 = 0.0625$. In Fig. 2a-b,d, when $T < T_c$, the external electric field can induce electrons to shift and break symmetry in the *b*-axis direction, forming some stable quasi-one-dimensional electromagnetic channels, ensuring the electromagnetic field energy to pass through without loss and forming superconducting current.

It must be noted that the long-range charge-ordered structures in Fig. 2 are ideal theoretical results. In experiments, due to non-uniform doping, different regions of a single superconducting sample can have different charge-ordered phases. Especially in extremely underdoped cases, because the charges are too dilute, the lack of effective interactions and competition prevents the formation of large-scale ordered structures, causing the electrons in the superconducting material to prefer forming short-range incommensurate clusters. Most recently, two research teams have discovered local nematic states with typical sizes of $4a_0 \times 4b_0$ as basic plaquettes using scanning tunneling microscopy (STM) techniques on (Bi2201)[34] and (CCOC)[35]. Interestingly, their results show that within each $4a_0 \times 4b_0$ unit, there are three nematic stripes with bright middle and two relatively dark sides. Here, we argue that the intrinsic double CuO_2 surfaces (α and β) inside copper-based superconductors probably induce this universal behavior that plaquettes with internal stripe-shaped patterns.

Fig. 3a shows the $4a_0 \times 4b_0$ plaquette cluster in CCOC with Na^{1+} atoms introduced to replace Ca^{2+} atoms resulting in the mirror symmetry breaking and hole doping of octahedral quantum wells. From the stability and symmetry perspectives, doping occurs in the central position of the upper CuO_2 layer, forming three connected octahedral quantum wells (α) with electrons that contribute to the central brightest bar in the STM experiment. Doping in the lower CuO_2 plane occurs at $\pm 1.5a_0$ positions, forming a pair of symmetrically arranged four connected octahedral quantum wells (β_1 and β_2). Due to the CuO_2 plane (β) is far from the cleavage plane ($h_\beta > h_\alpha$), two corresponding bars appear darker. According Fig. 3a, we

can qualitatively provide the theoretical result of DOS peaks as the magenta line in Fig. 3b; the intensity ratio of the central peak to the two secondary peaks can be determined quantitatively according to h_α and h_β. Assuming that the central peak is 1, then the values of the two secondary peaks are $k = h_\alpha/h_\beta$. It is known that the h_α and h_β of CCOC and Bi2201 are (2.742 Å, 10.263 Å) and (4.662 Å, 17.175 Å), respectively, and their ratio k is 0.267 and 0.271, respectively. Then, the value of the two secondary peaks is approximately 0.27, as indicated by the red dotted line in Fig. 3b. The experimental results for CCOC and Bi2201 are shown in green and blue in the figure, respectively. It is not difficult to see from Fig. 3b that the experimental results of Bi2201 are in good agreement with the theory, but there are errors in the position and intensity of the secondary peaks of CCOC. We analyze that these errors may be related to factors such as scanning speed and the distance between the probe and the sample surface.

Fermi surface Sheets, abnormal T_c and d-wave symmetry in Bi2223

It has been found that the maximum T_c value of cuprate superconductors is highly dependent on the number of CuO_2 planes within a structural unit and usually reaches the maximum at three layers. In the case of Bi2223 superconductor, two unusual behaviors have been identified: (1) In ARPES measurementsr, the majority of observations reveal one or two Fermi surface sheets[41–44]. However, a recent report has indicated the presence of three Fermi surface sheets[37], (2) its T_c remains nearly constant from optimal doping to the double optimal doping, whereas most superconductors experience a decrease in T_c with increasing doping in the over-doped regions[45]. Researchers investigated using a 6×6 Hamiltonian with 36 matrix elements to uncover the microscopic mechanism behind these two peculiar effects[37,44]. We argue that the explanation by introducing many adjustable parameters needs to be more convincing from the physical mechanism.
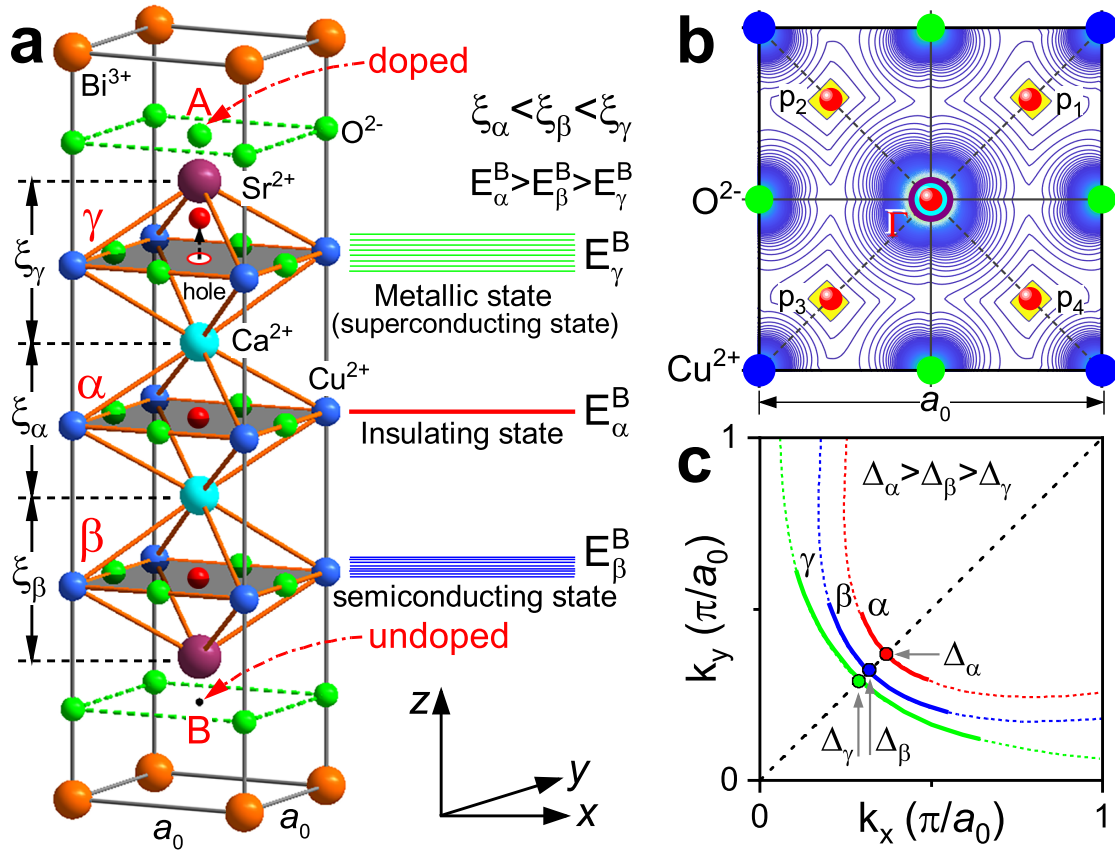
Figure 4. The relationship between quantum confinement effects and the Fermi arc in Bi2223 superconductors. **a**, Three kinds of octahedral quantum wells and their corresponding local electrons in real space coexist with three states (energy bands): insulating state (α), semiconducting state (β), and metal state (γ) . **b**, Numerical simulation shows there are two kinds of electrons (states) inside the CuO_2 unit cell: the strong correlation Γ-electron in the center, which is responsible for superconductivity with s-wave symmetry; the weak correlation p-electrons in four diagonal yellow pockets are responsible for normal photoelectrons in ARPES and other experiments with d-wave symmetry. **c**, Three split Fermi arcs correspond to the three kinds of confined pocket electrons.

In the new framework, the distance ξ between two vertices of the octahedron is a critical parameter, which not only determines whether the material can be superconducting and its superconducting transition temperature but also affects the structure of the Fermi surface. As shown in Fig. 4a, there are three octahedral quantum wells within a unit in the Bi2223 superconductor. The two vertices of α, β, and γ are (Ca^{2+}, Ca^{2+}), (Ca^{2+}, Sr^{2+}) and (Sr^{2+}, Ca^{2+}), respectively. In the case of undoped, β and γ are degenerate. Because the charges of the three octahedrons are symmetric and in balance, all electrons are shielded, and the superconductor behaves as an insulator.

The T_c of the Bi2223 superconductor can be tuned by oxygen doping, and both the A position of the upper oxygen layer and the B position of the lower oxygen layer may be occupied by doped oxygen ions (Fig. 4a). In the case of light doping, we assume that only the A site is doped, then β and γ are no longer degenerate, so there are three different kinds of octahedral quantum wells in the Bi2223 superconductor: the undoped intermediate α-plane (MP), the doped upper γ-plane (UP) and undoped lower β-plane (LP). Since the radius of Ca^{2+} (99 pm) is smaller than that of Sr^{2+} (113 pm), thus $\xi_\alpha < \xi_\beta$. In the case of γ, the doping of negative oxygen ion at the A site results in the decrease of the effective charge valence of Sr^{2+}, and the upward displacement of electrons leads to the stretching of ξ_γ and the mirror symmetry breaking of the octahedron along the c-axis. Hence, the ξ values of the three types of octahedrons in the Bi2223 superconductor satisfy the following relationship: $\xi_\alpha < \xi_\beta < \xi_\gamma$, which implies that the binding energies of the three confined electrons with corresponding octahedrons satisfy the inequality: $E_\alpha^B > E_\beta^B > E_\gamma^B$. As shown in the inset on the right side of Fig. 4a, three types of electrons (α, β, γ) in the Bi2223 superconductor form three energy bands, respectively. Because α electrons are insulating and do not participate in conduction and superconductivity, the corresponding extremely narrow energy band E_α^B is called the silent band or valence band. E_β^B is the semiconductor energy band to be doped, and the widest E_γ^B is the doped metal energy band or conduction band. This indicates that the metallic state (superconducting state), insulating state, and semiconducting state can coexist in the Bi2223 superconductor.

In the limit of weak doping, the physical properties of the Bi2223 superconductor are uniquely determined by the doped γ quantum well. Fig. 4b shows the numerical simulation of the Coulomb field inside CuO_2 unit cell in an octahedron. Two types of electrons or electronic states are confirmed in the octahedron: the first is Γ-electron located in the center of CuO_2, and the second is the p-electron situated in the yellow pockets of four diagonal directions of CuO_2. The Γ-electron is firmly combined with the octahedron that determines the material's superconducting properties. However, the p-electrons are weakly correlated to the octahedron due to the relatively weak restriction from the neighboring layers. When $T < T_c$, the electrons stay in the center Γ position, while $T > T_c$, they absorb heat energy and enter the pocket diagonally to become normal p-electrons. They can escape from the octahedron by absorbing photon energy, leaving the superconductor to become photoelectrons and appearing in the ARPES experiment. These photoelectrons accumulate over time to form a single green Fermi arc of Fig. 4c with a small energy gap Δ_γ. It must be pointed out that the physical meanings of E_γ^B and Δ_γ are entirely different, E_γ^B corresponds to superconducting energy and Δ_γ to pseudo-energy gaps of normal state. Moreover, it has been long debated whether the pairing symmetry of high-temperature superconductivity is d-wave or s-wave[46]; because superconducting Γ-electrons are localized in the central symmetry position, the corresponding E_γ^B shows isotropic s-wave symmetry[47], while for normal p-electrons, they can only appear in four diagonal pockets correspond to the 4-nodes, so they show d-wave symmetry. Hence, the so-called d-wave symmetry is merely the result of the localized electrons within the octahedron interacting with the nearest oxygen ions (negative charges) and the next-nearest copper ions (positive charges) in the CuO_2 plane, which is not directly related to superconducting properties.

In the case of overdoped samples, the crystal lattice distortion leads to the symmetry breaking of α and β polyhedrons, thus reducing the binding energy (E_α^B and E_β^B) between the confined electrons and the octahedrons. Hence, electrons from α and β octahedrons may also be excited into the corresponding four Fermi pockets and captured as photoelectrons by ARPES, as indicated by the red and blue Fermi arcs with energy gaps Δ_α and Δ_β in Fig. 4c, respectively. Because $\Delta_\alpha > \Delta_\beta > \Delta_\gamma$, with the increase of doping concentration, it is possible to observe one (γ), two (γ, β), or even three (γ, β, α) Fermi surface sheets in the ARPES experiment of the Bi2223 superconductor, as reported. In addition, the length of the Fermi arcs corresponding to different electrons is directly proportional to ξ and inversely proportional to Δ.

The second unusual behavior is why the maximum T_c of Bi2223 can persist in the overdoped region. This problem is relatively easy to explain qualitatively by using the new mechanism. Firstly, the middle CuO_2 plane formed by α octahedra is an insulating layer, and doping does not change its insulation characteristics. However, the UP and LP copper oxide surfaces isolated by the MP can independently exhibit superconductivity upon doping. Consequently, the three-layer structure of Bi2223 can be regarded as a dual superconductor. Initially, doping occurs solely in the UP, and when the doping reaches the optimal level (p $\simeq$ 0.16), the critical temperature T_c attains its maximum value in UP. As doping continues, the LP assimilates the excess carriers and enters a superconducting state. Meanwhile, the UP maintains its optimal doping state before the LP achieves its optimal level. As a result, the maximum value of T_c remains unchanged. Subsequently, when the LP also reaches the optimal doping, corresponding to a total doping concentration of 0.32, further doping at this stage leads to the simultaneous entry of excess carriers into both the UP and LP. Consequently, the optimal superconducting state is disrupted,

and the superconducting transition temperature declines.

Quantum confinement and Resonant modes in iron-based Superconductors

As the second class of high-T_c superconductors, iron-based have a lower critical temperature than copper-based superconductors. Understanding the similarities and differences between these two classes of superconductors is essential for developing a comprehensive theory of high-temperature superconductivity. The 1111 series represents the first family of iron-based superconductors discovered and currently boasts the highest superconducting transition temperatures. As shown in Fig. 5a-d, this series can be denoted as LnFeAsO, where Ln represents elements including La, Sm, Ce, Nd, Gd, and F, commonly substituting the O position. The FeAs layer is a crucial structural component in iron-based superconductors, and the superconducting behavior is closely associated with these FeAs layers. Copper-based superconductors exhibit a two-dimensional CuO_2 layer structure, and a class of octahedral is enough to describe their electronic behavior (Fig. 1). Whereas iron-based superconductors possess a folded sandwich structure of As-Fe-As, we find that two types of polyhedral quantum wells are needed to explain their electronic behavior.
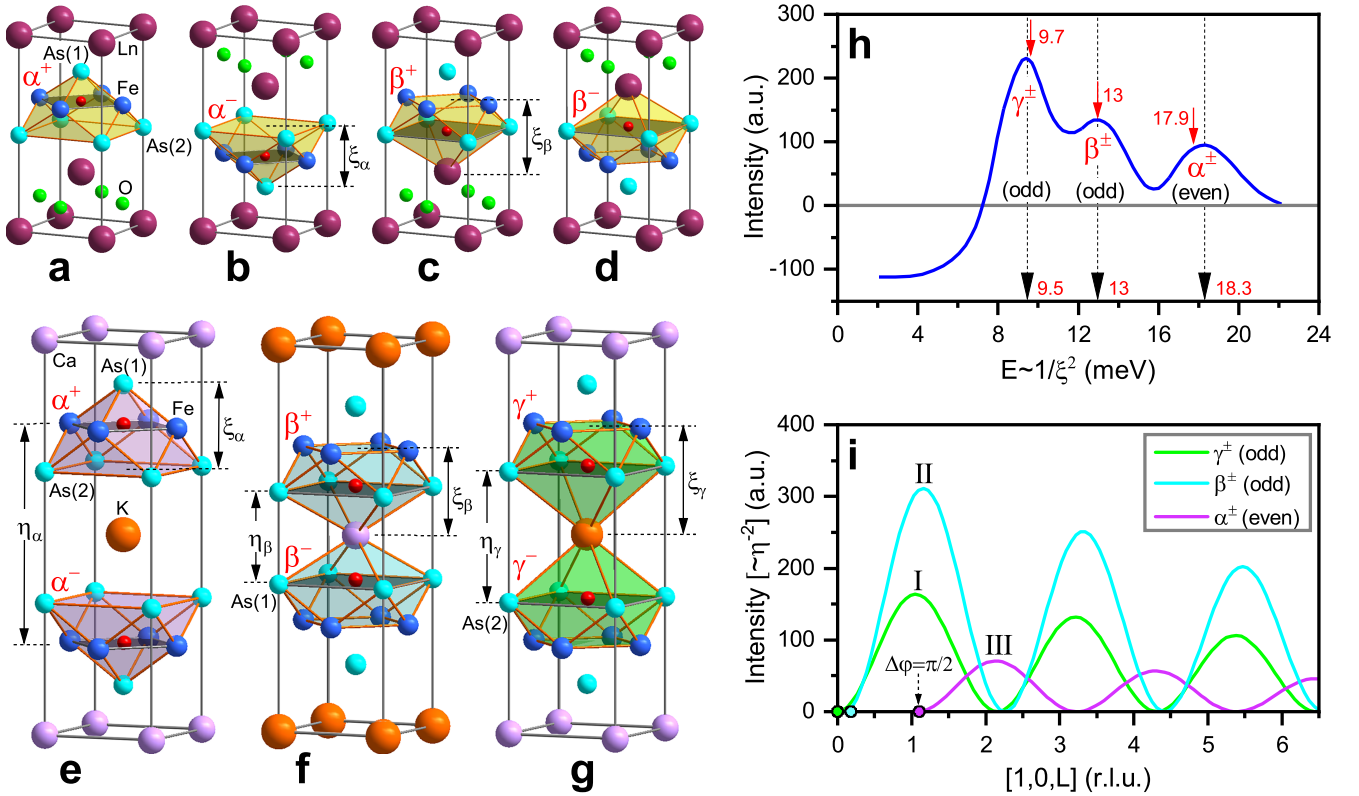
Figure 5. Polyhedral confined electrons, local Cooper pairs, and resonant modes in iron-based superconductors. $\mathbf{a-d}$, The nonahedron and the tri-decahedron confinement cages (quantum-well) in the iron-based 1111 superconductor. $\mathbf{e-g}$, Three real-space local Cooper-pair harmonic oscillators in CaKFe$_4$As$_4$ superconductor. $\mathbf{h}$, The experimental results of neutron spin resonance peaks correspond to three kinds of quantum well resonant cavities, and the height of resonant cavities determines the corresponding theoretical values. $\mathbf{i}$, The relationship between odd-even symmetry of resonance peaks of iron-based 1144 superconductor and the initial phase of harmonic oscillators.

Fig. 5a-d are the localized electronic state confined by two kinds of quantum wells in 1111 superconductors. Fig. 5a,b are the $\alpha^{\pm}$ phase of the nonahedron, and Fig. 5c,d are $\beta^{\pm}$ phase of tri-decahedron, where the electrons are localized at the center of iron and arsenic layer units, respectively. An interesting question arises: Can the height of the iron-based superconductors' polyhedral quantum wells (ξ_α and ξ_β in the Fig. 5b,c) determine the T_c of superconducting materials as the ξ in equation (1) of copper-based octahedron?

Table 2 shows the relationship between the superconducting transition temperature and the height of the polyhedra in iron-based superconductors. It can be observed that the majority of iron-based superconductors are dual-phase, while only the 1144 series exhibits three-phase coexistence. Comparing Table 1 and Table 2, the relation of T_c and quantum well parameter

Table 2. The relationship between T_c of iron-based superconductors and and the height ξ of polyhedral quantum well, the values in bold are possible superconducting phases.

Compound	T_c(K)	ξ_α (Å)	ξ_β (Å)	ξ_γ (Å)	λ
$LaFeAsO_{1-x}F_x$	43	2.6723	**3.0749**		406
$SmFeAsO_{1-x}F_x$[7]	43	2.7291	**3.0792**		407
$SmFeAsO_{1-x}F_x$[8]	55	**2.7149**	3.0433		405
$TbFeAsO_{1-x}F_x$	45	2.7567	**3.0501**		418
$GdFeAsO_{1-x}F_x$	53.5	**2.7454**	3.0568		403
$PrFeAsO_{1-x}F_x$	52	**2.6857**	3.0591		375
$NdFeAsO_{1-x}F_x$	50	**2.7227**	3.0418		371
$CeFeAsO_{1-x}F_x$	41	2.6930	**3.0777**		388
$LaFeAsO$	41	2.6608	**3.0912**		392
$LaYFeAsO$	42	2.6840	**3.0912**		401
$BaKFe_2As_2$	38	2.7650	**3.3242**		419
$CaKFe_4As_4$	35	2.5617	2.9276	**3.3874**	402
$KCa_2Fe_4As_4F_2$	33	2.8406	3.0301	**3.4353**	390
$K_{0.8}Fe_ySe_2$[39]	32		**3.534**		400
	48.7	**2.836**			393

ξ of copper-based and iron-based superconductors follow a similar law. However, their correlation strength coefficients are different, $\lambda(Cu)$=1300 for copper-based superconductors is approximately three times that of $\lambda(Fe)$=400 for iron-based superconductors. Surprisingly, the record T_c (164 K) of copper-based superconductors[5] is also three times that of iron-based superconductors (55 K)[8].

The double superconducting phase of iron-based superconductor was first experimentally verified in $SmFeAsO_{1-x}F_x$ of 1111 series. Table 2 shows that Chen et al. found the β-phase of 43 K at atmospheric pressure[7], while Ran et al. prepared α-phase of 55 K by high pressure[8]. Moreover, Fig. 5e-g shows three-phase structures in $CaKFe_4As_4$ of 1144 series, where three pairs of different quantum wells or resonant cavities can be constructed in the superconductor, with Fe, As(1), and As(2) as electron confined layers respectively. Since the radii of Ca, K, Fe, and As ions are R(Ca)=99, R(K)=138, R(Fe)=64, and R(As)=58 pm, respectively. Therefore, the height ξ of phases $\alpha^\pm$, $\beta^\pm$, and $\gamma^\pm$, composed of As(1)-Fe-As(2) (Fig. 5e), Fe-As(1)-Ca (Fig. 5f), and Fe-As(2)-K (Fig. 5g), respectively, satisfies the following relationship: $\xi_\alpha < \xi_\beta < \xi_\gamma$, which is confirmed by high-precision X-ray crystal structure data.

When the paired electrons are resonating inside the paired resonant cages, they always keep the vibration directions opposite, and the amplitudes are equal. According to Fig. 1b,c, the vibration process of an electron pair is equivalent to the periodic transition of spin-up and spin-down electron states. If momentum and spin are used to describe the vibration state of the paired electrons, which is identical to the definition of Cooper pairs made of two electrons of opposite spin and momentum. As shown in Fig. 5e-g, there are three intrinsic Cooper resonance electron pairs inside $CaKFe_4As_4$, and each contributes to one definite spin resonance mode; hence, the triple spin resonance modes can be found in the experiment (Fig. 5h)[38].

The resonance energy is directly proportional to the superconducting energy gap, which establishes a relationship between the resonance energy and the height of the polyhedron of Fig. 5e-g as follows:

$$E_j^R = \frac{\Theta}{\xi_j^2}, \quad j = \alpha, \beta, \gamma, \tag{3}$$

where Θ is the undetermined coefficient.

According to the crystal structure data[38], $c = 12.63$ Å and $zc = 5.855$ Å (the distance between adjacent Fe-Fe planes), resulting in $\xi_\alpha = 2.504$ Å, $\xi_\beta = zc/2 = 2.928$ Å, and $\xi_\gamma = (1-z)c/2 = 3.387$ Å. To determine the undetermined coefficient Θ, assuming the resonance peak E_β^R of phase $\beta^\pm$ is 13 meV, by applying equation (3) we can determine the two other resonance peaks of phase $\alpha^\pm$ and phase $\gamma^\pm$ as $E_\alpha^R = 17.9$ meV and $E_\gamma^R = 9.7$ meV, which are consistent with the experimental values of 18.3 meV and 9.5 meV, respectively.

As shown in Fig. 5i, the researchers found that two resonant modes with lower energy are odd modes with sine square modulation in space, while the other resonant mode with higher energy is an even mode with cosine square modulation in space, and pointed out that the peak intensity of resonance is inversely proportional to the energy gap. Academic circles generally believe that the parity of resonance modes in superconductors is due to the formation of two different modulation

modes of spin resonance modes in momentum space. We think the crux of the problem lies in the existence of three kinds of real-space quantum resonant cavities with different binding energies, and their interaction leads to parity.

When the neutrons enter the superconductor, the energy of the neutron is not absorbed by the three harmonic oscillators simultaneously, and the initial phases of their vibration are different because of the different orders of absorbing energy. As shown in Fig. 5i, the γ harmonic oscillators with the smallest binding energy are the easiest to start vibration by absorbing neutrons (I of the green line). Once the γ oscillators vibrate, they first affect the β oscillators with smaller binding energy, which are forced to begin vibrating (II of cyan line), and their initial phase is slightly delayed. The binding energy of the α harmonic oscillators is the largest, and the vibration of α cannot be triggered until the electrons in the γ harmonic oscillators are the closest to those in α and the Coulomb interaction between them is the largest, that is, the amplitude of the γ harmonic oscillator reaches the maximum. From the phase point of view, the initial phase of the α oscillators is just $\pi/2$ later than that of the γ oscillators (III of magenta line), so the parity difference of resonance modes emerges. We believe that parity embodies causality between different oscillators, with odd mode as cause and even mode as effect. This conclusion is reflected in the experiment: there is no vibration signal in the range of [0, 1] of the α harmonic oscillator (magenta line in Fig. 5i), which the experiment has ideally confirmed[38]. In addition, the intensity of the resonance peak mainly depends on the amplitude of electrons, and the energy gap will have a particular influence on the amplitude. However, the most significant impact comes from the distance between two electrons in the paired harmonic oscillator (η in Fig. 5e-g). According to the structural data $\eta_\alpha = 7.22$ Å, $\eta_\beta = 3.13$ Å, and $\eta_\gamma = 4.37$ Å, through the inverse relationship ($I \sim 1/\eta^2$), it can be estimated the odd mode's strength is about three times that of the even mode, which is also consistent with the paper's results[38].

Pressure-induced dual superconducting phase transition in $K_{0.8}Fe_ySe_2$

Pressure significantly influences the behavior of superconductors by inducing structural changes that can modify their electronic properties and impact superconductivity. In 2012, Sun et al. studied the effect of pressure on iron-based superconductors, particularly $K_{0.8}Fe_ySe_2$[39]. Surprisingly, they observed a second phase transition in superconductivity triggered by pressure. The experimental fact is the most favorable support for the hypothesis that two different polyhedral superconducting phases exist in the same iron-based superconducting material (Table 2). This finding challenges existing theories on superconductivity, suggesting the need for a new framework to explain the presence of multiple superconducting phases and their respective transition temperatures. The discovery emphasizes the importance of further exploration and a deeper understanding of superconductivity, which may pave the way for developing innovative superconducting theories.
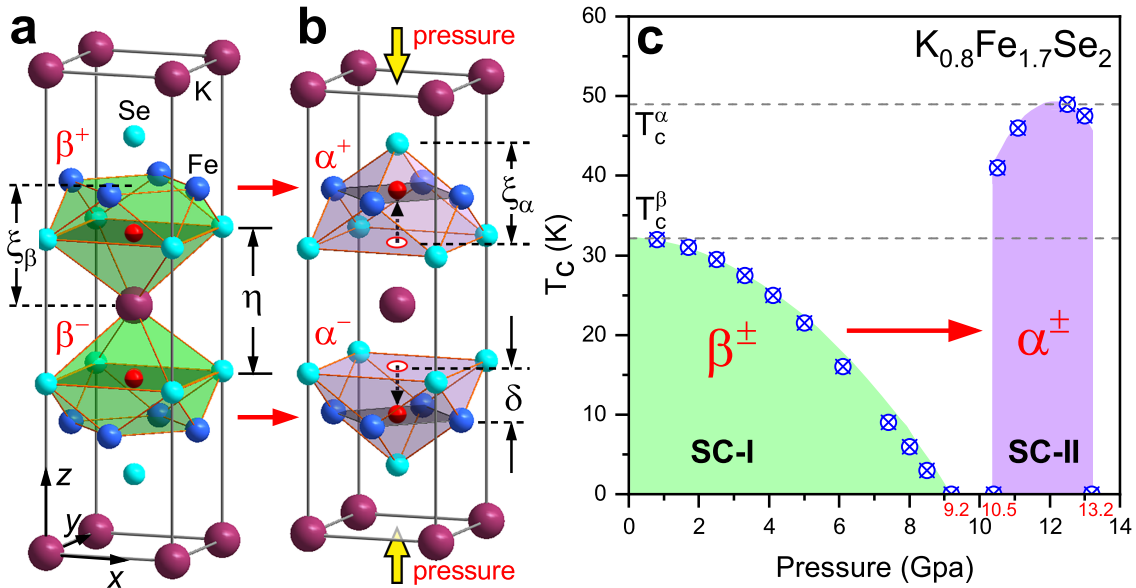
Figure 6. Illustrate the pressure-induced phase transition of intrinsic double superconducting phases in $K_{0.8}Fe_ySe_2$ superconductor. **a**, In the low-T_c superconducting $\beta^\pm$-phase, where local Cooper pairs are confined in the two Se layers of a pair of connected quantum wells. **b**, Under pressure, the localized electron transfer from two Se planes into two Fe planes and the emergence of high-T_c of the $\alpha^\pm$-phase. **c**, The variation of T_c with pressure in the superconductor, the double superconducting phases SC-I and SC-II correspond to the real-space Cooper electron states confined by the polyhedral quantum wells in **a** and **b**, respectively.

Next, we will show that the pressure-induced superconducting transition temperature mechanism can be well understood within the framework of confined Cooper pairs. As shown in Fig. 6a,b, similar to the 1111 series, two kinds of polyhedral quantum wells can be constructed inside the $K_{0.8}Fe_ySe_2$ superconductor. The lower T_c of the $\beta^\pm$ phase (SC-I) represented by Fig. 6a, and the higher T_c of the $\alpha^\pm$ phase (SC-II), represented by Fig. 6b. According to the crystal structure parameters of Table 2 ($\xi_\alpha = 2.836$ Å and $\xi_\beta = 3.534$ Å), the highest superconducting transition temperatures for the respective phases can be accurately predicted as $T_c^\beta = 400/\xi_\beta^2 \simeq 32.1$ K for $\beta^\pm$ phase and $T_c^\alpha = 400/\xi_\alpha^2 \simeq 49$ K for $\alpha^\pm$ phase. These two values closely match the experimentally observed highest transition temperatures, 32 K and 48.7 K, for the first and second superconducting phases (Fig. 6c)[39].

Under the new framework, we can reproduce the process of the superconducting electronic state change in the phase diagram of Fig. 6c. Before the pressure is applied, the real-space Cooper pairs are localized in two Se atomic layers of β^+ and β^- quantum wells (Fig. 6a), respectively, and at this time, the maximum $T_c = 32$ K. When external pressure is exerted in the direction of the z-axis, the distance η of the paired electrons will decrease, and the stability of the electrons will be reduced due to the stronger Coulomb repulsion between them, so will the T_c of the superconductor. With the pressure increase, both η and T_c will decrease monotonously and slowly until the displacement and symmetry breaking in the superconducting xy-plane are entirely suppressed, and the superconductor returns to its parent insulating phase. Increasing the pressure (9.2 Gpa$< p <$10.5 Gpa), although η of the paired electrons continues to decrease and the repulsive force gradually increases, they are still localized in their respective Se atomic layers, and the superconductor remains insulated.

As shown in Fig. 6b, when the pressure $p >$10.5 Gpa, the repulsive force between the paired electrons exceeds the binding force from $\beta^\pm$ octahedral quantum well, and the paired electrons in the upper and lower Se layers will instantly separate and then jump into the two nearest Fe atomic layers and recombine into $\alpha^\pm$ phase superconducting Cooper pairs with a higher T_c. Therefore, as the experiment observation, the phase transition from the insulating to superconducting state is abrupt. Now, the double superconducting phase transition is not mysterious. It is just the charge transfer of two paired electrons (real-space Cooper pair) under the Coulomb repulsion, and they are shifted upward and downward from the original equilibrium position of the Se local layer by $\delta \simeq 1.4$ Å (indicated by black arrows in Fig. 6b), respectively. When the pressure increases to 12.5 GPa, the newly paired electrons enter a stable state of force balance in the z-direction, and the corresponding T_c reaches a maximum of about 49 K. When the pressure reaches 13.2 GPa, the symmetry breaking of electrons in the three directions of xyz is wholly suppressed again, and the superconductor reenters an insulating state.

Conclusion and discussion

Beyond the conventional BCS paradigm, we have developed a theoretical framework for unconventional superconductors centered around visualized polyhedron quantum-well localized electrons. Using X-ray diffraction data, this real-space confinement mechanism can directly estimate the superconducting transition temperatures of copper-based and iron-based superconductors, which are entirely consistent with experimental results. To further verify and validate the effectiveness and reliability of the new superconducting scenario, an extensive study was conducted on various aspects such as charge-ordered states in STM experiments, Fermi surface structures in ARPES experiments, spin resonance peaks with parity symmetry in neutron spin resonance experiments, and pressure-induced dual superconducting phase transitions. Despite the vast differences between the superconductors and phenomena studied, it is compelling that the unified mechanism proposed in this work can flawlessly explain all experimental observations.

More recently, signatures of superconductivity have been observed in the $La_3Ni_2O_7$ with $T_c \simeq 80$ K under pressure above 14 GPa[9], sparking global scientific interest in superconducting research once more[48–50]. Of particular interest, the question arises: Will the highest transition temperature of Ni-based superconductors exceed that of Cu-based superconductors? Some theoretical results suggest that the T_c of Ni-based superconductors can surpass that of Cu-based superconductors and even realize room-temperature superconductivity[48]. Our work offers new insight into this question. According to the superconducting mechanism of local electrons, nickel-based superconductors, and copper-based superconductors have similar octahedral quantum well structures (Fig. 1a, Cu^{2+} are replaced by $Ni^{2.5+}$), where the value of $\xi = (0.5 - 0.316) \times 19.734 = 3.631$ Å[9], by substituting this value into equation (1), the highest superconducting transition temperature of Ni-based superconductors can be estimated at 100 K. Most recently, by partially replacing La with smaller Pr, Wang et al. obtained $La_2PrNi_2O_{7-\delta}$ samples with T_c of 82.5 K, which is about 2.5 K higher than that of $La_3Ni_2O_7$. We think this is because the smaller Pr leads to the contraction of ξ and, in turn, the increase of T_c. It is known that $R(La^{3+}) = 103$ pm and $R(Pr^{3+}) = 99$ pm, and the change of T_c caused by element replacement can be estimated as $\Delta T_c = 80 \times (R(La^{3+}) - R(Pr^{3+}))/R(La^{3+}) \simeq 3.1$ K, which is consistent with the experimental result of 2.5 K.

Moreover, it is noteworthy that trilayer cuprates exhibit the highest T_c among all cuprates, reaching up to 164 K under high pressure for mercury-based compounds[5]. This raises the question of whether trilayer nickelates display higher T_c superconductivity[49]. From Fig. 4, it is evident that the trilayer mercury-based cuprate can achieve higher T_c due to two crucial

factors: (1) octahedral quantum well with small ξ; (2) mirror symmetry breaking caused by oxygen doping. While trilayer Ni-based superconductors have similar types of octahedral quantum wells, but their ξ values are about ξ_α=3.698 Å and ξ_β=3.767 Å, which are much larger than the corresponding cuprates (about 3.211 Å). Because the T_c that can be improved by pressurization or simple element replacement is very limited, We conclude that it is unrealistic to expect the T_c of nickel-based superconductivity to surpass that of copper-based or even hope it can realize room-temperature superconductivity.

Our results indicate that the real-space local electronic framework enables the study of high-T_c striped superconductors and helps understand their unconventional superconducting phase transition behavior. We believe the proposed method holds immense potential for unraveling the mysteries underlying the strongly correlated systems.

Acknowledgements

References

1. Onnes, H. K. The Resistance of pure mercury at helium temperatures. *Leiden Comm.* **119b**, 122-130 (1911).

2. Bardeen, J., Cooper, L. N. & Schrieffer, J. R. Theory of superconductivity. *Phys. Rev.* **106**, 162-164 (1957).

3. Bednorz, J. G. & Müller, K. A. Possible high-T_c superconductivity in the Ba-La-Cu-O system. *Z. Phys.* B. **64**, 189-193 (1986).

4. Wu, M. K. et al. Superconductivity at 93 K in a new mixed-phase Y-Ba-Cu-O compound system at ambient pressure. *Phys. Rev. Lett.* **58,** 908-910 (1987).

5. Gao, L. et al. Superconductivity up to 164 K in $HgBa_2Ca_{m-1}Cu_mO_{2m+2+\delta}$ (m = 1, 2, and 3) under quasihydrostatic pressures. *Phys. Rev. B* **50**, 4260–4263 (1994).

6. Kamihara, Y., Watanabe, T., Hirano, M. & Hosono, H. Iron-based layered superconductor $La[O_{1-x}F_x]FeAs$ (x= 0.05-0.12) with T_c = 26 K. *J. Am. Chem. Soc.* **130**, 3296-3297 (2008).

7. Chen, X. H. et al. Superconductivity at 43 K in $SmFeAsO_{1-x}F_x$. *Nature* **453**, 761-762 (2008).

8. Ren, Z. A. et al. Superconductivity at 55 K in iron-based F-doped layered quaternary compound $Sm[O_{1-x}F_x]FeAs$. *Chin. Phys. Lett.* **25,** 2215-2216 (2008).

9. Sun, H. L. et al. Signatures of superconductivity near 80 K in a nickelate under high pressure. *Nature* **621**, 493–498 (2023).

10. Anderson, P. W. The resonating valence bond state in La_2CuO_4 and superconductivity. *Science* **235**, 1196-1198 (1987).

11. Dagotto, E. Correlated electrons in high-temperature superconductors. *Rev. Mod. Phys.* **66**, 763-840 (1994) .

12. Monthoux, P., Pines, D. & Lonzarich, G. G. Superconductivity without phonons. *Nature* **450**, 1177-1183 (2007).

13. Anderson, P. W. Is there glue in cuprate superconductors? *Science* **316**, 1705-1707 (2007).

14. Lee, P. A., Nagaosa, N. & Wen, X. G. Doping a mott insulator: physics of high-temperature superconductivity. *Rev. Mod. Phys.* **78**, 17-85 (2006).

15. Fradkin, E., Kivelson, S. A. & Tranquada, J. M. Colloquium: Theory of intertwined orders in high temperature superconductors. *Rev. Mod. Phys.* **87**, 457-482 (2015).

16. Tranquada, J. M., et al. Neutron diffraction from magnetic order in superconducting $La_{2-x}Sr_xCuO_4$. *Nature* **375**, 561-563 (1995).

17. Hoffman, J. E. et al. A four unit cell periodic pattern of quasi-particle states surrounding vortex cores in $Bi_2Sr_2CaCu_2O_{8+\delta}$. *Science* **295**, 466–469 (2002).

18. Kivelson, S. A. et al. How to detect fluctuating stripes in the high-temperature superconductors. *Rev. Mod. Phys.* **75**, 1201-1241 (2003).

19. Fischer, Ø., Kugler, M., Maggio-Aprile, I., Berthod, C. & Renner, C. Scanning tunneling spectroscopy of high-temperature superconductors. *Rev. Mod. Phys.* **79**, 353-419 (2007).

20. Eduardo, H. et al. Ubiquitous interplay between charge ordering and high-temperature superconductivity in cuprates. *Science* **343**, 393–396 (2014).

21. Qi, X. L & Zhang, S. C. Topological insulators and superconductors. *Rev. Mod. Phys.* **83**, 1057-1110 (2011).

22. Keimer, B., Kivelson, S. A., Norman, M. R., Uchida, S. & Zaanen, J. From quantum matter to high-temperature super-conductivity in copper oxides. *Nature* **518**, 179–186 (2015).

23. Zaanen, J. & Gunnarsson, O. Charged magnetic domain lines and magnetism of high-T_c oxides. *Phys. Rev. B* **40**, 7391–7394 (1989).

24. Mook, H. A., Dai, P., Dogan, F., & Hunt, R. D. One-dimensional nature of the magnetic fluctuations in $YBa_2Cu_3O_{6.6}$. *Nature* **404**, 729-731 (2000).

25. Srivats, R. et al. Probing optically silent superfluid stripes in cuprates. *Science* **359**, 575-579 (2018).

26. Berg, E., Fradkin, E., Kivelson, S. A., & Tranquada, J. M. Striped superconductors: how spin, charge and superconducting orders intertwine in the cuprates. *New J. Phys.* **11**, 115004 (2009).

27. Kondo, T. et al. Competition between the pseudogap and superconductivity in the high-T_c copper oxides. *Nature* **457**, 296-300 (2009).

28. Lawler, M. J. et al. Intra-unit-cell electronic nematicity of the High-T_c copper-oxide pseudogap states. *Nature* **466**, 347-351 (2010).

29. Shen, K. M. et al. Nodal quasiparticles and antinodal charge ordering in $Ca_{2-x}Na_xCuO_2Cl_2$. *Science* **307**, 901-904 (2005).

30. Kim, C. et al. Observation of anisotropic gap in the superconducting state of $YBa_2Cu_3O_{7-\delta}$. *Phys. Rev. Lett.* **77**, 4054-4057 (1996).

31. Croft, T. P., Lester, C., Senn, M. S., Bombardi, A. & Hayden, S. M. Charge density wave fluctuations in $La_{2-x}Sr_xCuO_4$ and their competition with superconductivity. *Phys. Rev. B* **89**, 224513 (2014).

32. Chang, J. et al. Direct observation of competition between superconductivity and charge density wave order in $YBa_2Cu_3O_{6.67}$. *Nat. Phys.* **8**, 871-876 (2012).

33. Komiya, S., Chen, H. D., Zhang, S. C., & Ando, Y. Magic doping fractions for high-temperature superconductors. *Phy. Rev. Lett.* **94**, 207004 (2005).

34. Ye, S. S. et al. Visualizing the Zhang-Rice singlet, molecular orbitals and pair formation in cuprate. Preprint at https://arxiv.org/abs/2309.09260 (2023).

35. Li, H. et al. Low-energy gap emerging from confined nematic states in extremely underdoped cuprate superconductors. *npj Quantum Mater.* **8**, 18 (2023).

36. Fernandes, R. M., Chubukov, A. V. & Schmalian, J. What drives nematic order in iron-based superconductors? *Nat. Phys.* **10**, 97-104 (2014).

37. Luo, X. et al. Electronic origin of high superconducting critical temperature in trilayer cuprates. *Nat. Phys.* **19**, 1841-1847 (2023).

38. Xie, T. et al. Odd and even modes of neutron spin resonance in the bilayer iron-based superconductor $CaKFe_4As_4$. *Phys. Rev. Lett.* **120**, 267003 (2018).

39. Sun, L. et al. Momentum-dependent electron dynamics and spin-fluctuation-driven superconductivity in $FeSe_{0.45}Te_{0.55}$. *Nature* **483**, 67-70 (2012).

40. Wu, T. et al. Magnetic-field-induced charge-stripe order in the high-temperature superconductor $YBa_2Cu_3O_y$. *Nature* **477**, 191-194 (2011).

41. Feng, D. L. et al. Electronic structure of the trilayer cuprate superconductor $Bi_2Sr_2Ca_2Cu_3O_{10+\delta}$. *Phys. Rev. Lett.* **88**, 107001 (2002).

42. Matsui, H. et al. BCS-like Bogoliubov quasiparticles in high-T_c superconductors observed by angle-resolved photoemission spectroscopy. *Phys. Rev. Lett.* **90**, 217002 (2003).

43. Kunisada, S. et al. Observation of Bogoliubov band hybridization in the optimally doped trilayer $Bi_2Sr_2Ca_2Cu_3O_{10+\delta}$. *Phys. Rev. Lett.* **119**, 217001 (2017).

44. Ideta, S. et al. Hybridization of Bogoliubov quasiparticles between adjacent CuO_2 layers in the triple-layer cuprate $Bi_2Sr_2Ca_2Cu_3O_{10+\delta}$ studied by angle-resolved photoemission spectroscopy. *Phys. Rev. Lett.* **127**, 217004 (2021).

45. Fujii, T., Terasaki, I., Watanabe, T. & Matsuda, A. Doping dependence of anisotropic resistivities in the trilayered superconductor $Bi_2Sr_2Ca_2Cu_3O_{10+\delta}$. *Phys. Rev. B* **66**, 024507 (2002).

46. Sigrist M. & Rice T. M. Unusual paramagnetic phenomena in granular high-temperature superconductors–A consequence of d-wave pairing? *Rev. Mod. Phys.* **67**, 503-513 (1995).

47. Zhu, Y. Y. et al. Presence of -wave pairing in Josephson junctions made of twisted ultrathin $Bi_2SrCaCu_2O_{8+x}$. *Phys. Rev. X* **11**, 031011 (2021).

48. Geisler, B. et al. Structural transitions, octahedral rotations, and electronic properties of $A_3Ni_2O_7$ rare-earth nickelates under high pressure. *npj Quantum Mater.* **9**, 38 (2024).

49. Zhu, Y. et al. Superconductivity in pressurized trilayer $La_4Ni_3O_{10-\delta}$ single crystals. *Nature* **631**, 531-536 (2024).

50. Wang, N. et al. Bulk high-temperature superconductivity in pressurized tetragonal La2PrNi2O7. *Nature* **634**, 579-584 (2024).